The NASA Ames PAH IR Spectroscopic Database: The Laboratory Spectra

A. L. Mattioda[1] , D. M. Hudgins[2], C. Boersma[1] , C. W. Bauschlicher, Jr.[3] , A. Ricca[1,4] , J. Cami[4,5,6] , E. Peeters[4,5,6] ,
F. Sánchez de Armas[4], G. Puerta Saborido[4], and L. J. Allamandola[1]

[1] NASA Ames Research Center, MS 245-6, Moffett Field, CA 94035, USA; Andrew.Mattioda@nasa.gov
[2] NASA Headquarters, MS 3Y28, 300 E St. SW, Washington, DC 20546, USA
[3] NASA Ames Research Center, MS 230-3, Moffett Field, CA 94035, USA
[4] Carl Sagan Center, SETI Institute, 189 N. Bernardo Avenue, Suite 200, Mountain View, CA 94043, USA
[5] Department of Physics and Astronomy, The University of Western Ontario, London, ON N6A 3K7, Canada
[6] The Institute for Earth and Space Exploration, The University of Western Ontario, London ON N6A 3K7, Canada

Abstract

The astronomical emission features, formerly known as the unidentified infrared bands, are now commonly ascribed to polycyclic aromatic hydrocarbons (PAHs). The laboratory experiments and computational modeling performed at NASA Ames Research Center generated a collection of PAH IR spectra that have been used to test and refine the PAH model. These data have been assembled into the NASA Ames PAH IR Spectroscopic Database (PAHdb). PAHdb's library of computed spectra, currently at version 3.20, contains data on more than 4000 species and the library of laboratory-measured spectra, currently at version 3.00, contains data on 84 species. The spectra can be perused and are available for download at www.astrochemistry.org/pahdb/. This paper introduces the library of laboratory-measured spectra. Although it has been part of PAHdb since its inception, the library of laboratory-measured spectra lacked a proper description in the literature. Here, the experimental methods used to obtain the data are described in detail, an overview of the contents of the experimental library is given, and specific tools developed to analyze and interpret astronomical spectra with the laboratory data are discussed. In addition, updates to the website, documentation and software tools since our last reporting are presented. Software tools to work with the spectroscopic libraries are being developed actively and are available at GitHub. Lastly, a comprehensive demonstration showing how the laboratory-measured data can be applied to explore absorption features in observations toward embedded sources is presented. This demonstration suggests that PAHs very likely contribute to interstellar absorption spectra associated with dense clouds and underscores the need for further IR spectroscopic studies of PAHs trapped in water ice.

Unified Astronomy Thesaurus concepts: Polycyclic aromatic hydrocarbons (1280); Astrochemistry (75); Interstellar dust (836); Astronomy databases (83); Astronomy data analysis (1858); Laboratory astrophysics (2004); Experimental techniques (2078)

1. Introduction

The family of emission features formerly known as the unidentified infrared (UIR) bands—discovered by Gillett et al. (1973) and attributed to molecular-sized species by Sellgren (1984)—are now generally attributed to polycyclic aromatic hydrocarbons (PAHs; e.g., Allamandola et al. 1989; Puget & Leger 1989; Peeters et al. 2004; van Dishoeck 2004; Draine & Li 2007; Tielens 2008; Li 2020, and references therein). The features that comprise this apparently universal spectrum contain a wealth of information about the astrophysical conditions in the emitting regions and the nature of their carriers (e.g., Joblin et al. 1994; Hony et al. 2001; Li & Draine 2001; Peeters et al. 2002; van Diedenhoven et al. 2004; Mulas et al. 2006; Bauschlicher et al. 2008, 2009; Galliano et al. 2008; Boersma et al. 2009, 2010; Mattioda et al. 2009, 2017; Ricca et al. 2010; Cruz-Diaz et al. 2019). However, exploitation of these features as astrophysical and astrochemical probes has been slow because the IR properties of PAHs under interstellar conditions were largely unknown for at least 20 years following their discovery.

From the early 1990s and onward, laboratory and computational data have been collected at NASA Ames Research Center to test and refine the hypothesis that large PAH molecules are responsible for the UIR bands (i.e., the PAH hypothesis). Initially these studies focused on small, easily acquired and well-studied PAHs (e.g., naphthalene, anthracene, etc.). In order to understand the influence of PAH structure on the UIR bands, PAHs containing five-membered rings, nitrogen atoms, and other structural features were investigated along with the impact of ionization. Since the number of potential PAH isomers grows rapidly with increasing PAH size (i.e., number of carbon atoms), studies were limited to those most thermodynamically stable. Similarly, as PAH sizes grow, their availability, both from an abundance and economic standpoint, diminishes. Later experimental studies focused on PAH species that would build up the fundamental foundation of PAH spectroscopy to compare and constrain computations.

However, to test the PAH hypothesis in full, these data need to be available to the larger astronomical community, along with the tools necessary to search and utilize them. The quantum-chemically calculated spectra span 2–2000 μm (5000–5 cm^{-1}; Bauschlicher et al. 2010, 2018; Boersma et al. 2014) and are included in the library of computed spectra, which is currently at version 3.20 and contains more than 4000 spectra. The experimentally determined spectra span 2–25 μm (5000–400 cm^{-1}) and are included in the library of laboratory-measured spectra, which is currently at version 3.00 and contains 84 spectra. The computed and laboratory-measured data provide complementary information. For example, the experimental data allow refinement and calibration of the computations, while the computations can provide spectra for
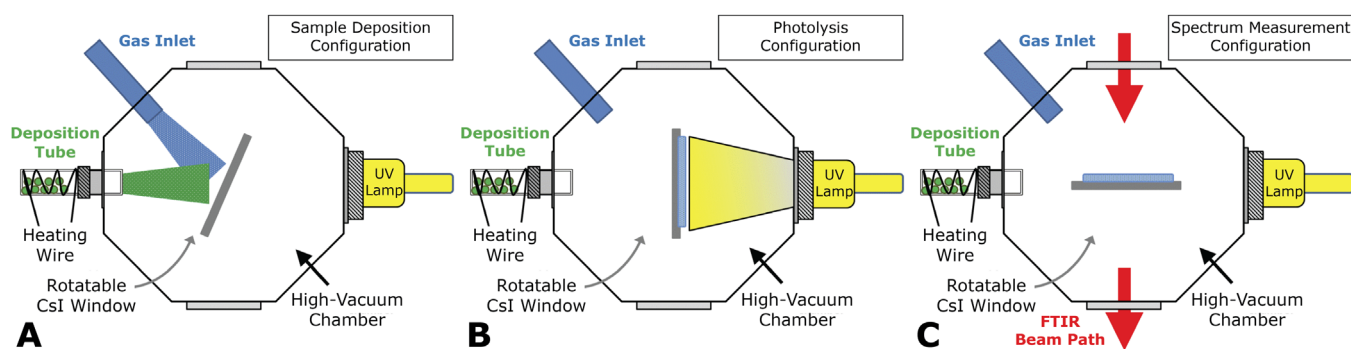
Figure 1. A typical setup for a matrix-isolation experiment: (A) sample deposition configuration, (B) UV photolysis configuration, and (C) configuration for collecting the IR spectrum.

PAH species that are not experimentally feasible assist in the assignment of bands, and identify experimental photoproducts. Furthermore, the laboratory-measured spectra contain information on overtone and combination bands, anharmonic effects, and electronic transitions in the mid-IR that are currently not included with the computed data (e.g., Mattioda et al. 2005a, 2005b, 2008). Laboratory experiments also offer opportunities for new discoveries. For example, the impact of nitrogenation on the C–C and C–H in-plane vibrational modes (e.g., Mattioda et al. 2003, 2008, 2017) and the identification of electronic transitions in the mid-IR (Weisman et al. 2005; Mattioda et al. 2014) were the result of pushing the PAH experimental envelope.

It would be remiss not to mention progress from other laboratory groups in the area of PAH IR spectroscopy. Studies of PAHs isolated in noble gas matrices have been conducted by a large number of groups in the astrophysical community, e.g., Vala et al. (1994), Garkusha et al. (2012). PAHs in the gas phase have been studied by, e.g., Joblin et al. (1995), Oomens et al. (2000), Kim et al. (2001), Cazaux et al. (2019) and those in encased in water ice by, e.g., Bouwman et al. (2011), Hardegree-Ullman et al. (2014), Cook et al. (2015), de Barros et al. (2017). Recently, the hypothesis that protonated PAHs contribute to the astronomical PAH bands was investigated by measuring the spectrum of protonated ovalene and coronene in para-hydrogen (p-H_2) matrices at 3.2 K by Tsuge et al. (2016), and references therein.

This paper focuses on the library of IR spectra of PAHs in argon matrices collected in the NASA Ames PAH IR Spectroscopic Database (PAHdb), currently at version 3.00, and describes the means by which the data were acquired. The data are accessible and downloadable at www.astrochemistry. org/pahdb/. The library of computed spectra have been described in detail in Bauschlicher et al. (2010), with adjustments and updates described in Boersma et al. (2014) and Bauschlicher et al. (2018). Online and offline tools are available for the user to work with the spectroscopic data in both libraries. Updates to the website, software tools and documentation made since the last reporting in Bauschlicher et al. (2018) are also discussed.

This paper is outlined as follows: Section 2 describes the experimental method used to derive the spectral information as well as (Section 2.1) and presents the library of laboratory-measured spectra (Section 2.4). Section 3 describes web access to this library and associated software tools. Section 4 demonstrates how the (software) tools can be used with the

library of laboratory-measured spectra to interpret astronomical observations. This paper is concluded in Section 5.

2. The Library of Laboratory-measured Spectra

In Section 2.1 a detailed account of the experimental methods is given. This is followed in Section 2.2 with a description of the physical units used and in Section 2.3 with a narration of the data analysis. Section 2.4 describes and breaks down the contents of the library of laboratory-measured spectra.

2.1. Experimental Methods

Neutral PAH molecules were isolated in an argon matrix that was prepared by vapor codeposition of the PAH of interest with an overabundance of argon (Ar) onto a 15 K CsI window suspended in a high-vacuum chamber (pressure between 10^{-7} and 10^{-8} Torr), as shown in the sample deposition configuration (Figure 1(A)). The PAH molecules are vaporized from heated deposition tubes, while argon is added via an adjacent N_2(l)-cooled gas inlet (Figure 1(A)). The deposition process is monitored via IR spectroscopy at 2 minute intervals (Figure 1(C)) and optimized to produce an Ar:PAH ratio in excess of 1000:1. A final IR spectrum of the PAH sample is recorded once a sufficient amount of PAH material is accumulated, which is determined by the strength (intensity) of the weakest bands (i.e., those in the 1400–1000 cm^{-1}; 7–10 μm C–C, C–H in-plane region).

The PAH samples, with a purity of at least of 99%, have been obtained from a variety of sources. Spectra were recorded using either a Bio-Rad/Digilab Excalibur FTS-4000 IR spectrometer that has been equipped with a MCT-B detector/ KBr broadband beam splitter or a Nicolet Analytical Instrument, Model 740 Fourier transform infrared (FTIR) spectrometer equipped with a MCT-B detector/KBr beam splitter combination. Spectra were recorded as the coaddition of 250–500 scans and at a resolution of 0.5 cm^{-1} with the CsI window rotated to the spectrum measurement configuration (Figure 1(C)).

Ionized PAH molecules are generated via *in situ* vacuum UV photolysis of the matrix-isolated neutral PAH (Figure 1(B)). The UV is produced by a microwave-powered flowing H_2 discharge lamp at a dynamic pressure of 150 mTorr, generating emission at 120 (Lyα; 10.2 eV) and 160 nm (7.8 eV). IR spectra are collected after 2, 4, 8, and 16 minutes of UV photolysis to aid in differentiating PAH ion bands from spurious photoproducts during analysis. The H_2 discharge

lamp's UV flux is $2.0 \pm 0.5 \times 10^{14}$ photons cm^{-2} s^{-1} (see Cruz-Diaz et al. 2019). Thus, during a 16 minute exposure PAH samples receive a dose of $\sim 2 \times 10^{17}$ UV photons. To be able to distinguish between bands arising from the PAH anion and cation, a second set of experiments are conducted in which the argon matrix is doped with an electron acceptor; either CCl$_4$ or NO$_2$ at a concentration of approximately 1:1200 relative to the argon gas. The electron acceptor quenches the formation of the PAH anion while enhancing that of the cation.

2.2. Physical Units: A-values

The library of laboratory-measured PAH spectra provides band positions (in cm^{-1}) and their associated strength (in km mol^{-1}; designated A-values here, which should *not* be confused with Einstein A coefficients). The use of A-values allows for a direct comparison with the data in the library of computed spectra and integration with tools developed for those data. Getting from laboratory measurements to A-values and their relationship with other physical parameters is outlined below.

First, consider a medium consisting of a uniform distribution of absorbers. A spectral flux $I_0(\nu)$ (W Hz^{-1}) passing through this medium will be attenuated by dI, proportional to $I_0(\nu)$. Second, the number of absorbers will be proportional to the thickness dl (cm) of the medium. Therefore one can write:

$$dI = -\kappa(\nu)I_0(\nu)dl, \qquad (1)$$

where $\kappa(\nu)$ (cm^{-1}) is the proportionality constant known as the absorption coefficient per unit volume. Integrating Equation (1) over the thickness, l, of the (uniform) medium yields:

$$\frac{I(\nu)}{I_0(\nu)} = e^{-\kappa(\nu)l}. \qquad (2)$$

The absorption coefficient per unit volume, $\kappa(\nu)$, is frequency dependent and encapsulates the nature and concentration of the absorber.

The laboratory experiments measure transmission T:

$$T(\nu) \equiv \frac{I(\nu)}{I_0(\nu)} \text{ and } A(\nu) = -\log_{10}(T(\nu)), \qquad (3)$$

where in molecular spectroscopy $A(\nu)$ is denoted the absorbance and is closely related to the optical depth $\tau(\nu)$ ($\equiv \kappa(\nu)l = A(\nu)/\log_{10}(e)$ for a uniform medium). From the laboratory data the strength of a PAH band is determined by integrating the measured absorbance, A (cm^{-1}), over the feature in wavenumber (ν_k; in cm^{-1}):

$$A = -\int_{\nu_k} A(\nu_k)d\nu_k. \qquad (4)$$

Since the absorption cross section $\sigma(\nu)$ (cm^2 molecule^{-1}) evaluates the absorption coefficient $\kappa(\nu)$ per unit volume, it is related to $A(\nu)$ through:

$$\sigma(\nu) = \frac{\kappa(\nu)}{n} = -\frac{A(\nu)}{N\log_{10}(e)} = -\frac{2.303A(\nu)}{N}, \qquad (5)$$

with n (cm^{-3}) the number of absorbers per unit volume and N ($\equiv nl$) the column density (cm^{-2}). Then, A-values are equated to the integrated cross section via:

$$A\text{-value} = \int_{\nu_k} \sigma(\nu_k)d\nu_k = \frac{2.303A}{N}, \qquad (6)$$
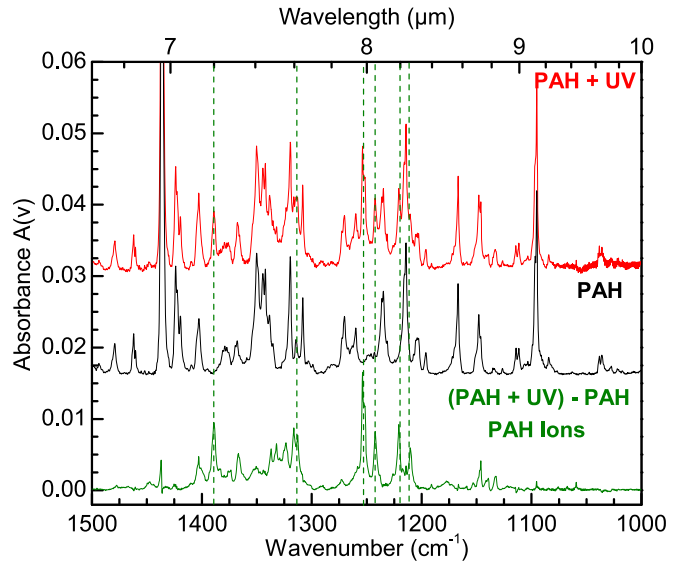
Figure 2. Comparison of pre- (black) and post- (red) photolysis PAH spectra and their difference spectrum (green) representing the PAH ions. The dashed lines indicate the strongest PAH ion bands, which are easily seen in the PAH + UV spectrum (red). The spectra shown are from the PAH '3,4;5,6;7,8-tribenzoperopyrene' (C$_{34}$H$_{16}$).

with the result given in units of km mol^{-1} or cm molecule^{-1}.

Lastly, it can be convenient to transform laboratory-measured A-values (km mol^{-1}) into cross sections integrated over frequency; $\sigma_{\nu,\text{int}}$ (cm^2 Hz). This can be achieved using the following relationship:

$$\sigma_{\nu,\text{int}} = \int_{\nu} \sigma(\nu)d\nu = 10^5 \frac{c \cdot A\text{-value}}{N_A}, \qquad (7)$$

where N_A is Avogadro's number and c (speed of light) is coming from the relationship $\nu = c\nu_k$.

The ability to discern and measure the strength of a band depends on the sensitivity of the FTIR spectrometer. Initial studies were conducted using an older model spectrometer that limited the detection to bands of at least 5 km mol^{-1} in strength. In the early 2000s a new FTIR spectrometer pushed this limit down to bands $\sim$2 km mol^{-1} in strength.

2.3. Analysis

Recorded spectra are first cleaned by removing contaminating bands due to water, CO$_2$, etc., baseline corrected, and, when necessary, filtered to remove fringing due to internal reflections in the sample window. Subsequently, additional baseline corrections are performed to remove undulations due to fringing caused by the thickness of the argon matrix. See also Hudgins et al. (1994), Mattioda et al. (2003, 2017), and references therein.

Upon UV irradiation only some 20% of the neutral PAHs are converted into ions. Thus, a single photolyzed spectrum (red spectrum in Figure 2) is a mixture of neutral, cation (positive ions), anion (negative ions) and miscellaneous photoproduct bands (e.g., CO$_2$, HAr$_2^+$). Bands originating from the PAH ions are identified by comparing the prephotolysis neutral spectrum to that measured after photolysis. Subtracting the neutral PAH spectrum from the photolyzed PAH spectrum produces a spectrum of the ion bands (green spectrum in Figure 2). Subsequently, bands are identified and their integrated absorbances plotted versus the UV photolysis time
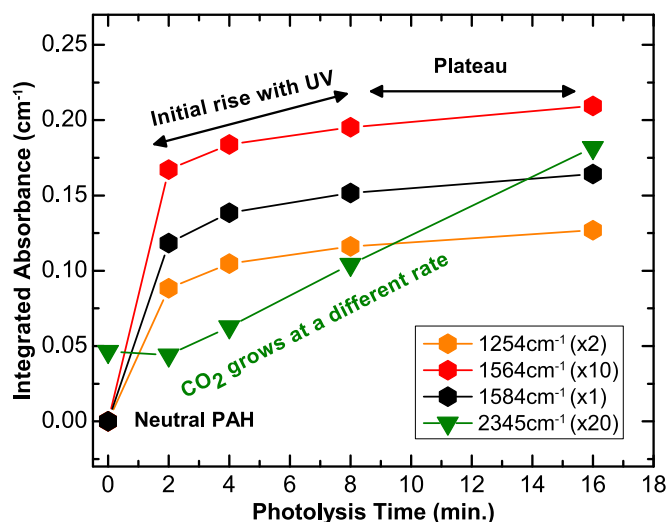
Figure 3. Evolution of three bands (black, red, and orange) of a given PAH ion photoproduct (at 1254, 1564, and 1584 cm^{-1}) compared to that of CO$_2$ (green at 2345 cm^{-1}) as a function of photolysis time. The PAH ion bands follow a distinct growth pattern characterized by a sharp increase followed by a plateau or slight decrease due to photobleaching, whereas the CO$_2$ band grows linearly. The bands have been scaled by a factor of 2, 10, and 20 for legibility.

(Figure 3). In such a plot PAH ions generally show an initial growth (first 2–8 minutes) before plateauing off or slightly decreasing due to photobleaching of the ions (Hudgins & Allamandola 1997; Hudgins & Sandford 1998a). Whereas, bands from other photoproducts show a different pattern, as is demonstrated in Figure 3 for CO$_2$. This CO$_2$ desorbs off the stainless steel walls of the vacuum chamber during UV photolysis freezing out on the sample window. Other potential photoproducts include HAr$_2^+$, with bands near 904 cm^{-1} (11.0 μm) and 1589 cm^{-1} (6.293 μm); CO$_2$ and CO desorbing from the stainless steel walls with bands near 2345 cm^{-1} (4.264 μm), 667 cm^{-1} (14.99 μm) and 2148 cm^{-1} (4.65 μm); and HO$_2^+$ with bands near 1388 cm^{-1} (7.204 μm) and 1104 cm^{-1} (9.058 μm; Hudgins & Allamandola 1995a). For a band to be ultimately assigned to the PAH cation it must also grow in the presence of the electron acceptor and do so in a fixed proportion to the other bands attributed to the cation.

To calculate A-values Equation (6) is used. However, the column density N cannot be independently determined from experiments. Therefore, it is obtained by scaling the sum of integrated absorbances (Equation (4); $A_{\mathrm{exp},i}$) determined for the neutral to the sum of computed A-values for its counterpart in the library of computed spectra (A-value$_{\mathrm{thy},i}$; Equation (8)). The advantage of using this approach is that while there can be some band-to-band variability in the computed A-values for individual bands, their sum is generally accurate to within 10%–20% (Hudgins & Sandford 1998a; Mattioda et al. 2003). For these sums, only bands falling between 1550 and 500 cm^{-1} (6.452–20.0 μm) are taken. The 500 cm^{-1} lower limit is chosen to exclude contributions from far-IR bands ($\nu_k < 500$ cm^{-1}). Whereas, the 1550 cm^{-1} upper limit is chosen to exclude the C–H stretching region, which can be overestimated at the level of theory used for the computed spectra (e.g., Langhoff 1996); to exclude potential contamination from bands due to matrix-isolated water near 1580–1700 cm^{-1} (5.88–6.33 μm); and to exclude overtone/combination bands between 1667–2000 cm^{-1} (5–6 μm) that are present in the measured spectra but not in those computed. The final A-values are obtained by scaling the

integrated absorbance of each band with the ratio of sums:

$$A\text{-value}_{\mathrm{exp},i} = A_{\mathrm{exp},i} \frac{\sum_j A\text{-value}_{\mathrm{thy},j}}{\sum_j A_{\mathrm{exp},j}}, \qquad (8)$$

with j for $1550 \geqslant \nu_j \geqslant 500$ cm^{-1}. Equation (6) is then used to obtain the column density (N) of the neutral PAH (see also Hudgins et al. 1994; Hudgins & Sandford 1998a).

For the ions it is assumed that the neutral PAHs that disappear during photolysis are all converted into ions. The relative loss in absorbance of all the neutral bands (Figure 2) multiplied with the column density determined for the neutral then yields the column density of the produced ions. The A-values for the ions are then simply calculated using Equation (6). A 50–50 split between anions and cations is made when there are bands that can be attributed to anions, which typically is only the case for larger PAHs. A 50–50 split is reasonable as the electron from the PAH cation will attach itself to the molecule/atom with the largest electron affinity, which is generally the neutral PAH in a PAH/argon matrix.

In certain cases, determining the A-values for ionized PAHs from spectra that have both cation and anion bands is complicated by their overlap, i.e., a mixed ion band. In those cases, the A-values for the cation are derived from the argon/NO$_2$ matrix data. The argon/NO$_2$ A-values also serve as a check on the A-values derived for the cation from the argon matrix data. The A-values for the anion of a mixed band are derived by taking the A-value of the mixed ion band and subtracting the A-value for the cation determined from the argon/NO$_2$ data.

For isolated bands, band positions are determined by locating its apex, i.e., highest point or peak. Easily discernible individual bands in band complexes are integrated separately, whereas complexes with no discernible individual bands are integrated in their entirety. The latter is often the case for bands in the C–H stretching region (3000–3100 cm^{-1}; 3.33–3.22 μm), but occasionally also for other regions of the spectrum, especially for large, irregular PAHs. In those cases, given the broad, overlapping bands, only a single band position and A-value is reported, with the largest intensity peak position being assigned as the identifier. Thus, the reader is advised to consult the experimental spectrum and/or the original publication when comparing or fitting the experimental C–H stretching region to astronomical observations. This issue will be remedied in a future update of the database. The reader is referred to the original publication (see Table 3 in Appendix A) for details pertaining a particular species. It should be noted that publications of experimental data prior to 2000 only reported relative intensities for the absorption bands instead of A-values. A-values for these species were calculated after their publication in the literature, using the original data and previously discussed methods. As such, these A-values are only available in the database and not in the published literature.

2.4. Contents of the Library of Laboratory-measured Spectra

The A-values from 84 spectra from a large variety of PAHs are available in the current version (version 3.00) of PAHdb's library of laboratory-measured PAH spectra. Table 3 (Appendix A) provides a list of the corresponding PAHs currently available in the database as well as their individual references.

The earlier versions 1.00 and 2.00 contained the spectra of 60 and 75 PAH species, respectively. For most PAHs, A-values are

Table 1
Breakdown of the Molecules in Version 3.00 of the Library of Laboratory-measured Spectra by Charge, Composition and Size

	Number of Carbon Atoms					
	1–10	11–20	21–30	31–40	41–50	Total
Charge	*All molecules*					
all	1(0)	43(3)	16(6)	14(0)	10(0)	84(9)
neutral	1(0)	23(3)	10(5)	8(0)	8(0)	50(8)
anion −	0(0)	1(0)	2(1)	3(0)	0(0)	6(1)
cation +	0(0)	19(0)	4(0)	3(0)	2(0)	28(0)
	PAHs with only carbon and hydrogen					
all	1(0)	23(0)	12(2)	14(0)	10(0)	60(2)
neutral	1(0)	12(0)	6(1)	8(0)	8(0)	35(1)
anion −	0(0)	0(0)	2(1)	3(0)	0(0)	5(1)
cation +	0(0)	11(0)	4(0)	3(0)	2(0)	20(0)
	PAHs with nitrogen					
all	0(0)	20(3)	4(4)	0(0)	0(0)	24(7)
neutral	0(0)	11(3)	4(4)	0(0)	0(0)	15(7)
anion −	0(0)	1(0)	0(0)	0(0)	0(0)	1(0)
cation +	0(0)	8(0)	0(0)	0(0)	0(0)	8(0)

Note. The difference in the number of entries between versions 2.00 and 3.00 is given in parentheses.

Figure 4. Breakdown of the PAHs in the library of laboratory-measured spectra by composition and number of carbon atoms. "Pure" PAHs contain only carbon and hydrogen; nitrogen refers to PAHs containing nitrogen as well. The cross-hatched areas indicate the additions between versions 2.00 and 3.00.

Figure 5. Breakdown of the PAHs in the library of laboratory-measured spectra by charge and number of carbon atoms. The cross-hatched areas indicate the additions between versions 2.00 and 3.00.

Figure 6. Distribution of PAH charge and composition in version 3.00 of the library of laboratory-measured spectra in percentages. *Nitrogen* refers to PAHs containing one or two nitrogen atoms in the hexagonal framework and *pure* refers to PAHs comprised solely of carbon and hydrogen.

available for both the neutrals and cations, with a smaller number for anion species. This smaller number is primarily due the fact that the smaller PAHs that dominate the library of laboratory-measured spectra have a relatively lower electron affinity when compared to larger PAHs and, as such, do not form anion bands during experiments. Version 3.00 corrects an issue where the data for the anion data for some molecules were inadvertently replicated in place of the cation data. This impacts the species with UIDs (unique identifiers) 540 and 541, 542 and 543, 546 and 547, and 549 and 550. In addition, the missing anion data of dibenzo[fg,st]pentacene was added (UID 813).

While "pure" PAHs comprised of only carbon and hydrogen dominate the library, PAHs containing nitrogen are also available. Table 1 shows the distribution of molecules in the library of laboratory-measured spectra, broken down by size, charge, and composition. In addition, the table indicates the changes between the prior version (2.00) of the library and the latest (3.00), and shows that seven of the nine newly added species are PAHs containing nitrogen (Mattioda et al. 2017). The information in Table 1 is presented graphically in Figures 4 and 5, which show the size breakdown by composition and charge, respectively. Figure 6 summarizes the charge and PAH type distribution of PAHs in two pie charts.

The species in version 3.00 of the library span a large size range (6–50 carbon atoms), with most falling in the 11–20 carbon atom range. The majority of species are neutral, while anions comprise less than 10%. However, the latter number is anticipated to increase when spectra from larger PAHs, which more readily form anions, are added. The library also holds, for a select number of species, the laboratory-measured absorbance spectra (see Figure 2). Given the complexities with overlapping anion/cation bands, NO_2 bands in the laboratory-measured absorbance spectra for the cations, etc. (see Section 2.3), a pure laboratory anion spectrum is not feasible. Therefore, the library holds the laboratory-measured UV photolyzed argon matrix absorbance spectrum and the UV

photolyzed argon/NO_2 matrix spectrum (i.e., cations only), where the neutral features have been removed via subtraction. This allows for the direct comparison of the laboratory-measured photolyzed argon matrix spectrum with that of the photolyzed argon/NO_2 matrix spectrum.

Figure 7. Screenshot illustrating the available information in the library of laboratory-measured spectra for neutral coronene, illustrating the contents and presentation at the website.

To allow comparison between the various neutral and ion spectra, the laboratory-measured absorbance spectra are normalized to 1×10^{16} molecules using the number of absorbers n determined from Equation (5). This normalization also corrects for any variations in total photon flux experienced during the generation of PAH ions.

3. Website, Tools, and Documentation

The laboratory-measured spectra can be perused and downloaded at the PAHdb website, which also offers online tools that allow users to compare/contrast the data as well as convert the laboratory-measured absorption spectra into emission spectra. Software tools to work offline with the downloaded library are available on GitHub and are actively developed. What follows, in turn, is a description of the website, software tools, and documentation; focusing on their connection with the library of laboratory-measured spectra and updates/improvements made since those reported in Bauschlicher et al. (2018).

Website Features and Tools—As an illustration of the type of information available for each species, Figure 7 presents a screenshot of the database website showing the information in the library of laboratory-measured spectra on neutral coronene ($C_{24}H_{12}$). The presentation of spectroscopic data is illustrated in Figure 8, which shows a table with the band positions and integrated cross sections (*A*-values; see Equations (6) and (7)) obtained from the absorbance spectrum shown on the right. A number of tools are available to work with these data, with the recent addition of the option to use Drude line profiles to synthesize spectra. Drude line profiles are, for example, employed by Smith et al. (2007) to model the dust features in their PAHFIT spectral analyses tool. The tool that allows fitting imported astronomical spectra is currently only available when the library of computed spectra ("Theory") is used. Lastly, each laboratory species has been linked to its computed counterpart. One can easily switch between the two (see Figure 7) and they can be directly compared, as is demonstrated in Figure 9.

Details | Transitions | Download

Transitions

Frequency [wavenumbers]	Wavelength [microns]	Integrated cross-section [km/mol]
3067	3.261	192.6
1923	5.2	7.224
1910	5.235	9.03
1896	5.274	9.03
1808	5.531	3.492
1799	5.56	1.746
1784	5.606	5.237
1768	5.657	1.746
1719	5.818	7.224
1696	5.898	7.224
1621	6.17	7.224
1579	6.332	1.746
1530	6.534	3.492
1505	6.643	5.237
1498	6.676	1.746
1317	7.591	55.99
1137	8.795	19.26
857	11.67	174.6

Laboratory Spectrum
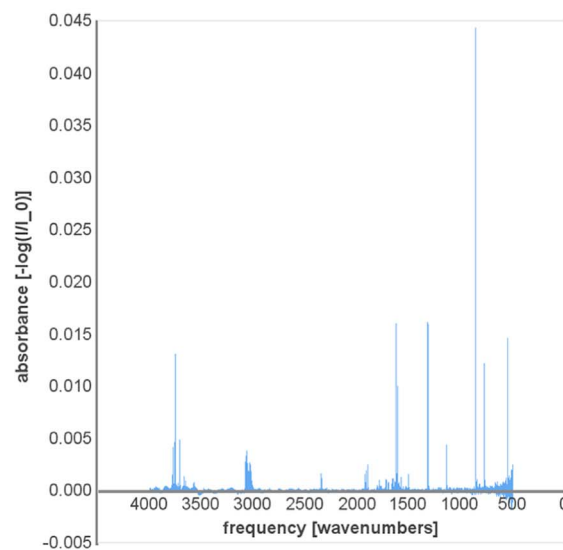
This spectrum was measured using the matrix isolation technique. Samples are prepared by co-deposition of the PAH in the gaseous state with an overabundance of argon onto a cold CsI window suspended in a high vacuum chamber (p ~ 10-8 mtorr). The CsI window temperature is held between 10 and 15 K for the duration of the experiment. The infrared spectrum of the cold CsI window is recorded prior to (I_0) and immediately after sample deposition (I_n). The absorbance spectrum for a neutral, matrix isolated PAH is log(I_n/I_0).

Figure 8. Screenshot of the website demonstrating the "transitions window" for the PAH coronene. See Sections 3 and 4 for details.

Software Tools—Three software tools (opposed to website tools) are under active development at GitHub. The first, and most mature, is the *AmesPAHdbIDLSuite*[7] and is described in Boersma et al. (2014). The most recent version of the *AmesPAHdbIDLSuite* is dated 2020 April 15, which constitutes a significant update.

Figure 10 demonstrates how the laboratory-measured *absorption* data for neutral coronene is synthesized into an *emission* spectrum (code in Lst. 1 in Appendix B), which subsequently can be used for comparison with astronomical observations. The employed emission model uses the cooling law described by Bakes et al. (2001) and parameters given in their Tables 3 and 4 for PAH neutrals and cations, respectively. The heat capacity needed for the calculations is computed using the group additive approach by Stein (1978) that was further worked out by Dwek et al. (1997) and only requires the laboratory-measured data; see also the appendix of Bauschlicher et al. (2010). The reader is informed that in most astronomical applications a $15 \, \mathrm{cm}^{-1}$ redshift is applied to account for some of the effects associated with emission. However, recent work by Mackie et al. (2018) has put some doubt on the need of such a correction in emission. Figure 11 shows the absorbance spectrum measured for neutral coronene.

With the rise of the use of Python in astronomical research and notably the STScI embracing it for their Analysis Toolkit to be used with the James Webb Space Telescope (JWST), the development of software tools has moved to Python. The *AmesPAHdbPythonSuite*[8] is set to offer the same features as the IDL suite using the same application programming interface.

In the advent of JWST, the PAHdb Team is developing the *pyPAHdb*[9] Python package as part of the Early Release Science program "Radiative Feedback from Massive Stars as Traced by Multiband Imaging and Spectroscopic Mosaics" (ID 1288; Peeters et al. 2018). The pyPAHdb has been described in detail in Shannon & Boersma (2018).

Documentation—Significant strides have been made in streamlining and improving PAHdb's documentation. Complete and accurate documentation is necessary for users to take full advantage of the data and tools that are offered. The online documentation describing the website has been updated to reflect recent changes and the website tour was brought online to reflect recent updates to the website. A cookbook with recipes for data analysis is being put together as well as videos covering PAH-related subjects, website usage, and data analyses with the software tools. The documentation can be found via the newly set up PAHdb Documentation Portal.[10]

4. Astronomical Application

Astronomical PAHs are typically observed in emission from UV-rich environments ($T_{\mathrm{gas}} = 10^2$–10^4 K; e.g., Peeters et al. 2002;

---

[7] github.com/PAHdb/AmesPAHdbIDLSuite

[8] github.com/PAHdb/AmesPAHdbPythonSuite

[9] https://github.com/PAHdb/pyPAHdb

[10] https://PAHdb.github.io

Comparing Experiment with Theory
Comparing experimental and theoretical spectra.
Species (1): $C_{24}H_{12}$
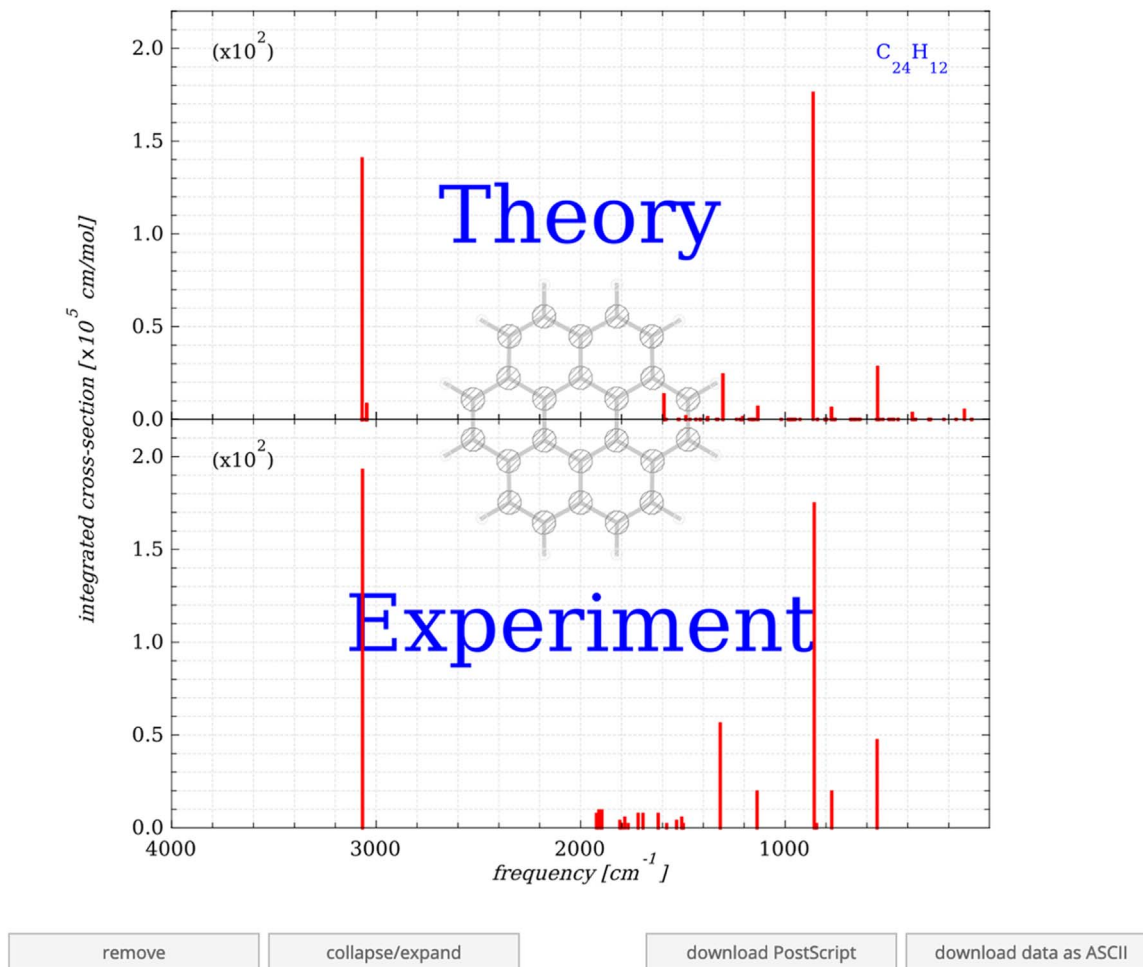
Figure 9. Screenshot of the website demonstrating the "results window" comparing the laboratory-measured and computed spectrum from theory for the PAH coronene. See Sections 3 and 4 for details.

van Diedenhoven et al. 2004; Tielens 2008). However, toward a few young stellar objects (YSOs; $T_{gas} \sim 10^2$ K) the 3.3 μm band has been observed in *absorption* (e.g., Sellgren et al. 1994; Brooke et al. 1996, 1999; Bregman et al. 2000; Keane et al. 2001). Observations toward embedded YSOs ($T_{gas} \sim 10$ K) reveal multiple varying absorption components contributing to the PAH regions of the spectrum (Schutte et al. 1996a, 1996b; Keane et al. 2001; Boogert et al. 2004, 2008), some of which could be explained by PAHs that are very likely encased in water ice. While the example given in Section 2.4 (Figure 10; code in Appendix B) focused on synthesizing a PAH *emission* spectrum from the laboratory data for comparison with astronomical observations, when comparing to spectra toward such embedded sources, no emission model is needed. Arguably, the raw laboratory-measured spectra themselves could directly be used, however, many of them can contain a mixture of charge states and artifacts due to contamination from other species (see Section 2.3). Furthermore, using the derived band positions and A-values instead of raw spectra allows for taking advantage of existing tools developed for the library of computed spectra.

To demonstrate this approach, the Infrared Space Observatory/ Short Wavelength Spectrometer (Kessler et al. 1996; Leech et al. 2003) spectrum toward the embedded protostar W33A (Gibb et al. 2000), which is presented in Figure 12, is briefly explored. The figure shows that the spectrum has strong absorption features, dominated by those from water ice and silicates. These features are subsequently removed following the procedures outlined in Boogert et al. (2008, 2011). The resulting residual spectrum shows two strong absorption features positioned at 6.0 and 6.85 μm, together with some smaller absorption bands. While ice species contributing to these features have been identified, they are unable to fully explain them (e.g., Boogert et al. 2015). This is especially true for the 6.85 μm feature, for which salts, organic residues, NH_4^+ and PAHs have been suggested as potential contributors (e.g., Keane et al. 2001; Boogert et al. 2008, 2015). Despite the PAHs, encased in water ice, showing band positions that are shifted 1–6 cm^{-1} and an overall $\sim$15% decrease in intensity when compared to matrix-isolated PAHs (see de Barros et al. 2017), argon matrix-isolated PAH data provide a good first estimate and can be used to assess the
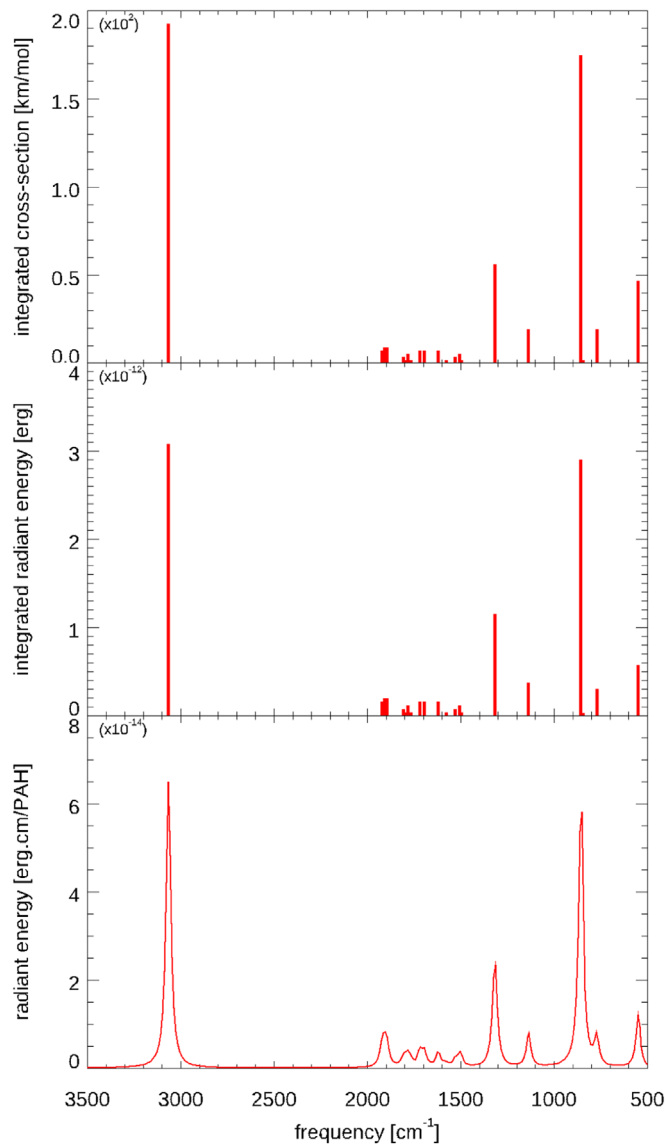
Figure 10. Converting the neutral laboratory-measured coronene *A*-values into an *emission* spectrum for comparison with astronomical observations. The code to generate the panels is shown in Lst. 1 in Appendix B. Top: *A*-value *absorption* spectrum of neutral coronene. Center: Stick *emission* spectrum of neutral coronene after it absorbs 7 eV, reaching 1494 K, and following the entire cooling cascade as per Bakes et al. (2001). Bottom: Synthesized *emission* spectrum of coronene demonstrating the use of the newly added Drude line profile (FWHM = 30 cm^{-1}) to the *AmesPAHdbIDLSuite*. See Section 3 for details.

Figure 11. The laboratory-measured absorbance spectrum of neutral coronene. The code to generate the figure is shown as part of Lst. 1 in Appendix B. See Section 3 for details.
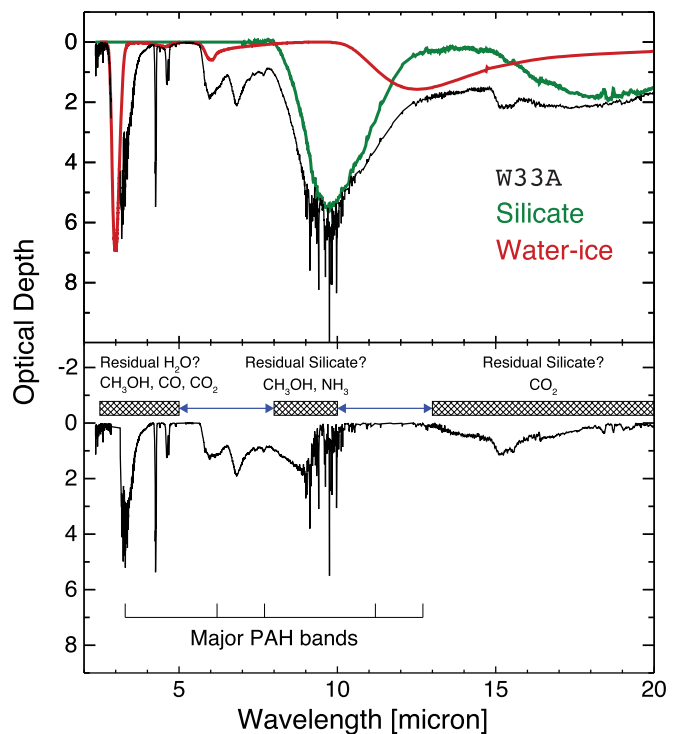
Figure 12. The 2–20 μm optical depth spectrum toward W33A. Top: original (black curve) showing a model fit to the H$_2$O ice (red) and silicate (green) absorption features. Bottom: the residual spectrum after removal of the H$_2$O ice and silicate contributions. Rectangular hashed regions indicate wavelength regions excluded from fitting due to their overlap with other ice and/or dust features. The blue arrows bracket the wavelength region of interest. Astronomical data and models are from Boogert et al. (2008). The positions of the prominent astronomical PAH *emission* features have been indicated.

potential presence of PAHs in water ice toward embedded sources.

Therefore, the residuals between 5–8 and 10.25–13 μm regions without definite feature assignments are fitted using synthesized 0 K spectra constructed from the laboratory data in PAHdb, i.e., from the determined band positions and their measured *A*-values. The *AmesPAHdbIDLSuite* is employed to construct the PAH absorption spectra and do the fitting, which uses a nonnegative least-squares approach (Lawson & Hanson 1974). Gaussian line profiles with a FWHM of 30 cm^{-1} are taken to generate the spectra—the broad extended wings associated with Lorentzian and Drude profiles cause the fits using those to perform less well and the 30 cm^{-1} FWHM simply gives the best match. The total band profile, both its width and shape, is affected by the diversity of the

PAH mixture. From the standpoint of the limited number of species in the library of laboratory-measured spectra, each individual PAH is considered as representing a statistical set of similar species with comparable peak centroids that are presumed to be distributed randomly around a mean with some FWHM. Furthermore, since bands from entirely different species also overlap, the fits presented here preclude the identification of specific PAHs, conforming PAHdb-fits to *emission* spectra (see e.g., Boersma et al. 2013).
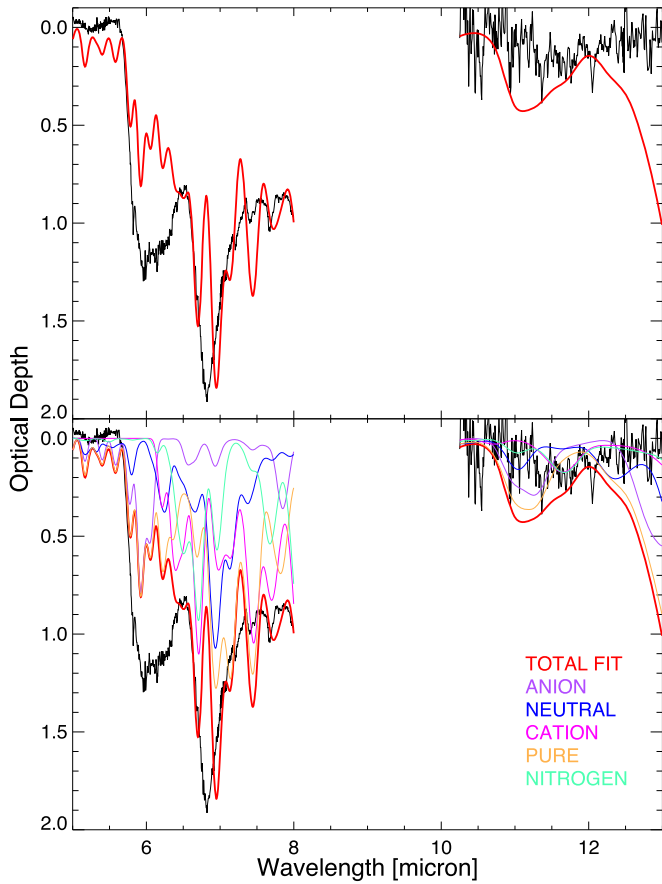
Figure 13. Top: the residual 5–8 and 10.25–13 μm optical depth spectrum toward W33A after removal of contributions from water and silicate (black curve) fitted with a mixture of PAHs (red). Bottom: the breakdown of the fit in terms of charge and composition as indicated by the different colored curves. See Section 4.1 for details.

Figure 14. Chemical structures of the 14 PAH species contributing to the PAHdb-fit of the ISO-SWS spectrum toward W33A. Hydrogen, carbon, and nitrogen are indicated by white, black and red, respectively. Indicated beneath each species' chemical structure is its chemical formula and its contribution to the total fit in terms of abundance (a) in percent. See also Table 2 and Section 4.1 for details.

4.1. Results and Discussion

The results of the PAHdb-fit are presented in Figure 13, with the chemical structure of the 14 contributing species and their share of the total fit in Figure 14. Figure 13 shows that the salient features of the spectrum can readily be reproduced. However, the quality of the fit leaves much to be desired, with significant discrepancies around 6 μm and beyond $\sim$12 μm. What these fits suggest is that PAHs can contribute to these features and thereby contribute to the chemistry taking place in and on interstellar ice grains. The bottom panel of Figure 13 and Table 2 show the breakdown of the fit in terms of charge and nitrogen and reveal that the emission is split 50–50 between both neutrals and cations and pure versus nitrogen-containing PAHs. Inclusion of nitrogen in PAHs is deemed highly plausible as it does not affect their stability (Hudgins et al. 2005), nitrogen is abundant in the environments where PAHs are thought to form (Buss et al. 1991; Speck & Barlow 1997; Boersma et al. 2006), and PANHs have been detected in meteorites (e.g., Hayatsu et al. 1977). Though, compared to *emission* studies (e.g., Rosenberg et al. 2011, 2014), the contribution from nitrogen here is large.

While the size of the library of laboratory-measured spectra does not permit for a direct assessment of the robustness of the fit in similar terms as when using the library of computed spectra (see, e.g., Boersma et al. 2013; Andrews et al. 2015), by extrapolating the fitted spectrum to extend to the regions

Table 2
Breakdown (%) of the PAHdb-fit to the ISO-SWS Spectrum toward W33A

Charge			Composition	
Anion	Neutral	Cation	Pure	Nitrogen
1.1	53.6	45.3	53.3	46.7

omitted for the initial fit one can check whether incompatible absorption has been generated. This is what is done in Figure 15, which shows that this is not the case as neither the 3.3 and 8–10 μm absorption exceeds that observed.

Another check is evaluation of the fraction of cosmic carbon that is locked up by the fitted PAHs. The absolute contribution of each fitted PAH is a direct measure of its column density. Multiplying this by the number of carbons in the PAH then gives the column density of carbon atoms locked up. Subsequently, taking the sum over each fitted PAH gives the total column density, which yields 1.0×10^{20} cm^{-2}. With a hydrogen column density toward W33A of 2.8×10^{23} cm^{-2} (Tielens et al. 1991) this translates into a carbon abundance of 3.6×10^{-4}, which is considerably higher than the available cosmic carbon abundance of $2.40(\pm 0.50) \times 10^{-4}$ (Cardelli et al. 1996). The obvious explanation for this discrepancy
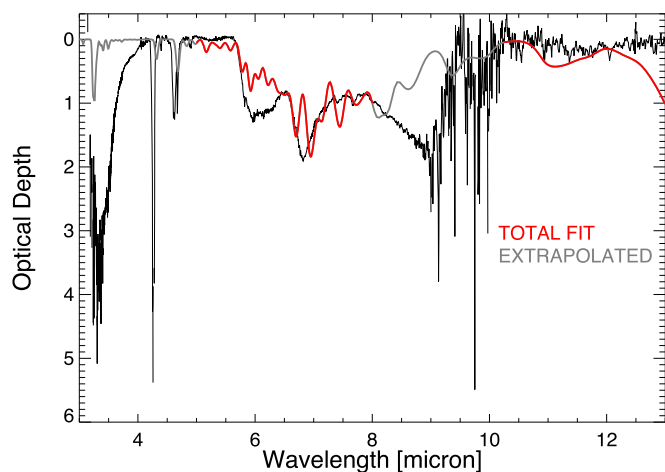
Figure 15. Extrapolation and comparison of the fitted PAH mixture to the entire 3–13 μm optical depth spectrum toward W33A, with the optical depth spectrum shown in black, the extrapolated spectrum in gray, and the fitted part of the spectrum in red. See Section 4 for details.

would be that other ice species contribute to the fitted spectral region as well.

Ongoing projects to extend the content of the library of laboratory-measured spectra could help put this type of analysis on a more solid footing. Notably the addition of spectra from PAHs in water ice, as, indeed, PAHs should efficiently condense out onto dust grains in cold environments (i.e., $T_{gas} \sim 10$ K), either as pure solids or as guest molecules in icy grain mantles, such as the case is for most other interstellar molecules (e.g., Sandford & Allamandola 1993; Hardegree-Ullman et al. 2014). The spectroscopy of PAHs in water-rich mixed molecular ices is still developing, but this preliminary exploration does show that at least some of the absorption could be explained by PAHs that are not very perturbed in an ice or perhaps in the gas phase (see Schutte et al. 1996b). Thus, as discussed in detail by Cook et al. (2015) and de Barros et al. (2017), this analysis strongly suggests that PAHs contribute to interstellar ice absorption spectra.

5. Summary

The family of astronomical emission features at 3.3, 6.2, 7.6, 7.8, 8.6, 11.2, and 12.7 μm, formerly known as the unidentified infrared bands, are now generally attributed to PAHs and PAH-related species. Laboratory experiments and computational modeling at NASA Ames Research Center generated a large collection of PAH IR spectra relevant for testing, developing, and refining the PAH model. These data have been collected into a spectroscopic database. The database libraries now contain over 4000 PAH spectra spanning 2–2000 μm (5000–5 cm^{-1}) for the quantum-chemically computed data and 84 spectra for the laboratory-measured data, spanning 2–22 μm (5000–450 cm^{-1}).

This paper describes the library of laboratory-measured spectra, the experimental setup and procedures used to analyze the data, updates to the database website located at www.astrochemistry.org/pahdb, improved and new software tools made available at GitHub, and enhanced documentation that can be reached via the new PAHdb Documentation Portal at

https://PAHdb.github.io. Lastly, a comprehensive demonstration is given showing how the laboratory-measured data, in conjunction with the *AmesPAHdbIDLSuite*, can be used to explore anomalous absorption in the ISO-SWS spectrum observed toward W33A. This demonstration indicates that PAHs could indeed contribute to interstellar ice absorption spectra, but also that more data on PAHs in water ice are needed to put such an application on firm footing.

First time users downloading data from the website may provide contact information, to be apprised when updates, such as new data and tools, become available. We also ask those who make use of the data and tools provided through the NASA Ames PAH IR Spectroscopic Database to refer to this work, Bauschlicher et al. (2010, 2018), and Boersma et al. (2014).

The contents of the PAHdb libraries are continuously expanded and will be extended to include spectroscopic data on PAH clusters, gas-phase measured PAH spectra, and mid-IR electronic transition. The software tools are being further developed to include more advanced PAH emission models (e.g., to include multiphoton absorption; Bakes et al. 2001; Montillaud et al. 2013; Andrews et al. 2015) and alternative fitting approaches (e.g., Bayesian). Thus far, PAHdb has proven to be an invaluable resource for astronomers to analyze and interpret astronomical PAH spectra obtained by past and current observatories and should do the same for the future, notably with the launch of JWST.

Appendix A
Available Data

Table 3 gives an overview of the 84 species in version 3.00 of the library of laboratory-measured PAH spectra. All spectra were collected at a temperature of 15 K ($\pm$3 K). The table contains the unique identifier (UID) assigned to each molecular species in PAHdb.

Table 3
Species in the Library of Laboratory-measured PAH Spectra
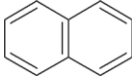
Structure	Formula	Name	Charge	UID	References
	$C_{10}H_8$	Naphthalene	0, +[*]	330	Hudgins & Sandford (1998a), Hudgins et al. (1994)
	$C_{13}H_9N$	7,8-benzoquinoline	0, +	274, 275	Mattioda et al. (2003)
	$C_{14}H_{10}$	Phenanthrene	0, +	273, 365	Hudgins & Sandford (1998a), Hudgins & Allamandola (1995a)
	$C_{14}H_{10}$	Anthracene	0, +	265, 266	Hudgins & Allamandola (1995b)
	$C_{13}H_9N$	Acridine	0	487	Mattioda et al. (2017)
	$C_{12}H_8N_2$	Phenazine	0, +, −	267, 268, 269	Mattioda et al. (2005c)
	$C_{16}H_{10}$	Fluoranthene	0, +[*]	387	Hudgins & Sandford (1998b), Hudgins et al. (2000)
	$C_{16}H_{10}$	Pyrene	0, +	334, 360	Hudgins & Sandford (1998a), Hudgins & Allamandola (1995a)
	$C_{15}H_9N$	2-azapyrene	0, +	271, 272	Mattioda et al. (2003)
	$C_{18}H_{12}$	Tetracene	0, +	282, 283	Hudgins & Sandford (1998a), Hudgins & Allamandola (1997)
	$C_{18}H_{12}$	Chrysene	0, +	291, 292	Hudgins & Sandford (1998a)
	$C_{17}H_{11}N$	1-azachrysene	0, +	293, 294	Mattioda et al. (2003)
	$C_{17}H_{11}N$	2-azachrysene	0, +	295, 296	Mattioda et al. (2003)
	$C_{17}H_{11}N$	4-azachrysene	0, +	297, 298	Mattioda et al. (2003)
	$C_{18}H_{12}$	1,2-benz[a]anthrancene	0, +	280, 281	Hudgins & Sandford (1998a), Hudgins & Allamandola (1997), Mattioda et al. (2017)
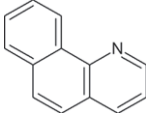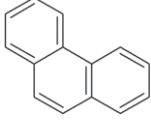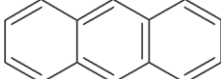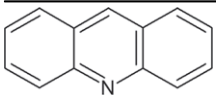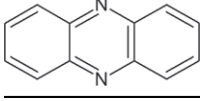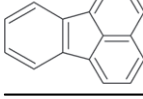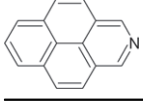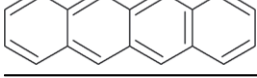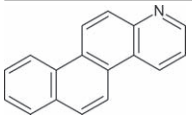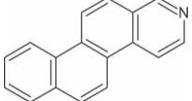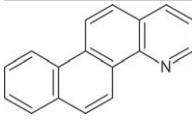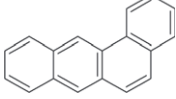
Table 3
(Continued)
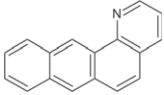
Structure	Formula	Name	Charge	UID	References
	$C_{17}H_{11}N$	1-azabenz[a]anthracene	0, +	285, 286	Mattioda et al. (2003)
	$C_{17}H_{11}N$	2-azabenz[a]anthracene	0, +	287, 288	Mattioda et al. (2003)
	$C_{17}H_{11}N$	Benz[a]acridine	0	831	Mattioda et al. (2017)
	$C_{17}H_{11}N$	Benz[c]acridine	0	830	Mattioda et al. (2017)
	$C_{20}H_{12}$	Benzo[e]pyrene	0, +	343, 367	Hudgins & Sandford (1998c), Hudgins & Allamandola (1995a)
	$C_{20}H_{12}$	Benzo[j]fluoranthene	0, +	395, 396	Hudgins & Sandford (1998b), Hudgins et al. (2000)
	$C_{20}H_{12}$	Benzo[k]fluoranthene	0, +	393, 394	Hudgins & Sandford (1998b), Hudgins et al. (2000)
	$C_{20}H_{12}$	Benzo[b]fluoranthene	0, +	391, 392	Hudgins & Sandford (1998b), Hudgins et al. (2000)
	$C_{20}H_{12}$	Benzo[a]fluoranthene	0, +	389, 390	Hudgins & Sandford (1998b), Hudgins et al. (2000)
	$C_{22}H_{14}$	Pentacene	0, +	307, 308	Hudgins & Allamandola (1995b), Hudgins & Sandford (1998b)
	$C_{22}H_{12}$	Benzo[g,h,i]perylene	0	284	Hudgins & Sandford (1998c), Hudgins & Allamandola (1995a)
	$C_{22}H_{14}$	Dibenz[a,j]anthracene	0	305	Mattioda et al. (2017)
	$C_{21}H_{13}N$	Dibenz[c,h]acridine	0	309	Mattioda et al. (2017)
	$C_{21}H_{13}N$	Dibenz[a,j]acridine	0	311	Mattioda et al. (2017)
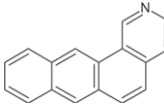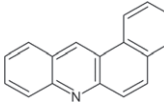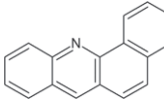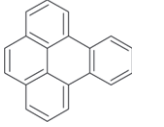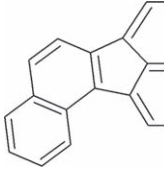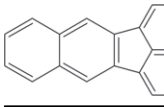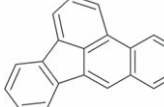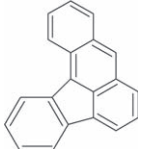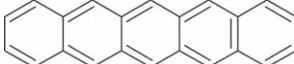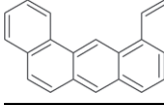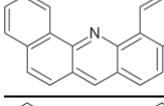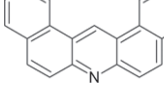
Table 3
(Continued)
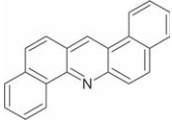
Structure	Formula	Name	Charge	UID	References
	$C_{21}H_{13}N$	Dibenz[a,h]acridine	0	303	Mattioda et al. (2017)
	$C_{21}H_{13}N$	Dibenz[a,c]acridine	0	833	Mattioda et al. (2017)
	$C_{24}H_{12}$	Coronene	0, +	18, 19	Hudgins & Sandford (1998c), Hudgins & Allamandola (1995a)
	$C_{24}H_{14}$	Dibenzopyrene	0, +, −	538, 549, 550	Mattioda et al. (2014)
	$C_{28}H_{16}$	Benzo-naptho-pyrene	0, +, −	537, 548, 813	Mattioda et al. (2014)
	$C_{32}H_{18}$	Dinapthopyrene	0, +, −	536, 546, 547	Mattioda et al. (2014)
	$C_{34}H_{16}$	3,4;5,6;7,8-tribenzoperopyrene	0	125	A. L. Mattioda et al. (2020, in preparation)
	$C_{36}H_{20}$	Naptho-anthraceno-pyrene	0, +, −	534, 542, 543	Mattioda et al. (2014)
	$C_{36}H_{16}$	3,4;5,6;7,8;12,13-tetrabenzoperopyrene	0	128	A. L. Mattioda et al. (2020, in preparation)
	$C_{36}H_{16}$	3,4;5,6;10,11;12,13-tetrabenzoperopyrene	0	154	A. L. Mattioda et al. (2020, in preparation)
	$C_{40}H_{22}$	Dianthraceno-pyrene	0, +, −	533, 540, 541	Mattioda et al. (2014)
	$C_{40}H_{18}$	Dipyreno-(1′,3′;10,2), (1″,3″,5,7)-pyrene	0	555	A. L. Mattioda et al. (2020, in preparation)
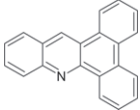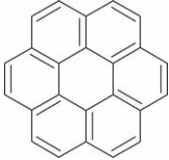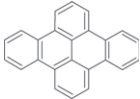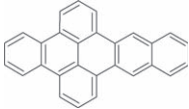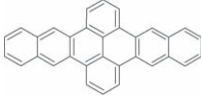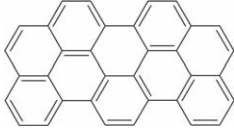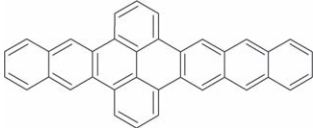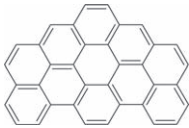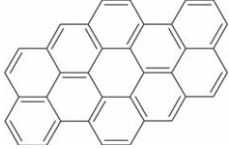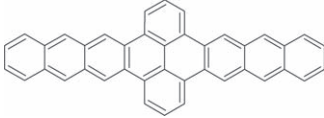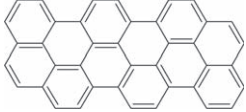
Table 3
(Continued)

Structure	Formula	Name	Charge	UID	References
	$C_{40}H_{18}$	12,13-o-phenylene-3,4;5,6;7, 8-tribenzoperopyrene	0	131	A. L. Mattioda et al. (2020, in preparation)
	$C_{42}H_{18}$	Hexabenzocoronene A	0, +	105, 106	Hudgins & Sandford (1998c)
	$C_{42}H_{18}$	1,14-benzodinaptho-(1″,7″;2,4), (7″,1″;11,13)-bisanthene	0	134	A. L. Mattioda et al. (2020, in preparation)
	$C_{42}H_{22}$	2,3;12,13;15,16-tribenzoterrylene	0	137	A. L. Mattioda et al. (2020, in preparation)
	$C_{44}H_{20}$	1,2;3,4;5,6;7,8;9,10;12, 13-hexabenzoperopyrene	0	140	A. L. Mattioda et al. (2020, in preparation)
	$C_{48}H_{20}$	Dicoronylene	0, +	100, 101	Hudgins & Sandford (1998c)
	$C_{48}H20$	Difluoranthen-(3′,5′;4,6), (4″,6″;9,11)-coronene	0	146	A. L. Mattioda et al. (2020, in preparation)
	$C_{48}H_{22}$	12,13-o-phenylene-1,2;3,4;5,6;7,8;9, 10-pentabenzoperopyrene	0	143	A. L. Mattioda et al. (2020, in preparation)
	$C_{50}H_{22}$	1,14-benzodiphenanthreno-(1″,9″;2,4), (9″,1″;11,13)-bisanthene	0	149	A. L. Mattioda et al. (2020, in preparation)
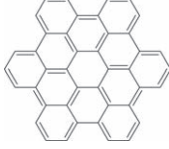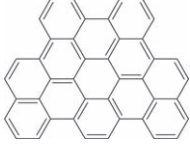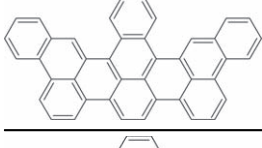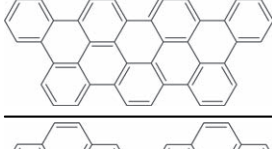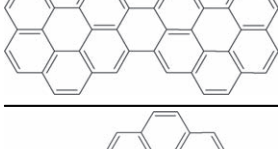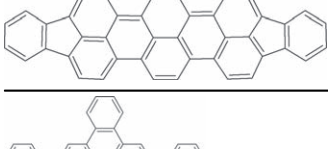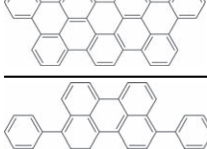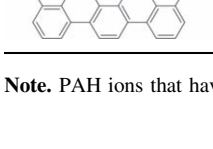
Note. PAH ions that have data available in the literature and will be uploaded to PAHdb in a future update have been indicated by a[*].

Appendix B
AmesPAHdbIDLSuite Code

Listing 1 provides the *AmesPAHdbIDLSuite* code used to create Figures 10 and 11 in Section 3.

Listing 1. *AmesPAHdbIDLSuite* code used to create Figures 10 and 11.

```
; read-in a library of laboratory-measured spectra from a downloaded
; XML-file
xml_file = 'pahdb-complete-experimental-v3.00.xml'
pahdb = OBJ_NEW('AmesPAHdbIDLSuite', Filename=xml_file)
; get the transitions for neutral coronene (UID = 18)
```

(Continued)

```
transitions = pahdb->GetTransitionsByUID(18)
; plot the stick spectrum of neutral coronene –Fig. 10, top
transitions->Plot
; calculate the emission spectrum of neutral coronene after it
; absorbs 7 eV using the approach set out in Bakes et al. (2001)
transitions->Cascade,7D*1.602D-12, /Approximate
; plot the resulting stick spectrum of neutral coronene after it
; absorbed 7 eV and following the entire emission cascade –Fig. 10,
; middle
transitions->Plot
```

(Continued)

```
; convolve the bands with a Drude line profile having a FWHM of 30
; /cm
spectrum=transitions->Convolve(FWHM=30D, /Drude)
; plot the emission spectrum of neutral coronene –Fig. 10, bottom
spectrum->Plot
; get the raw laboratory spectrum for neutral coronene (UID = 18)
laboratory = pahdb->getLaboratoryByUID(18)
; plot the raw laboratory spectrum of neutral coronene –Fig. 11
laboratory->Plot
; clean up after ourselves
OBJ_DESTROY, [laboratory, spectrum, transitions, pahdb]
```

ORCID iDs

A. L. Mattioda ● https://orcid.org/0000-0003-1153-7850
C. Boersma ● https://orcid.org/0000-0002-4836-217X
C. W. Bauschlicher, Jr. ● https://orcid.org/0000-0003-2052-332X
A. Ricca ● https://orcid.org/0000-0002-3141-0630
J. Cami ● https://orcid.org/0000-0002-2666-9234
E. Peeters ● https://orcid.org/0000-0002-2541-1602

References

Allamandola, L. J., Tielens, G. G. M., & Barker, J. R. 1989, ApJS, 71, 733
Andrews, H., Boersma, C., Werner, M. W., et al. 2015, ApJ, 807, 99
Bakes, E. L. O., Tielens, A. G. G. M., & Bauschlicher, C. W. 2001, ApJ, 556, 501
Bauschlicher, C. W., Boersma, C., Ricca, A., et al. 2010, ApJS, 189, 341
Bauschlicher, C. W., Peeters, E., & Allamandola, L. J. 2008, ApJ, 678, 316
Bauschlicher, C. W., Peeters, E., & Allamandola, L. J. 2009, ApJ, 697, 311
Bauschlicher, C. W., Jr., Ricca, A., Boersma, C., & Allamandola, L. J. 2018, ApJS, 234, 32
Boersma, C., Bauschlicher, C. W., Allamandola, L. J., et al. 2010, A&A, 511, A32
Boersma, C., Bauschlicher, C. W., Ricca, A., et al. 2014, ApJS, 211, 8
Boersma, C., Bregman, J. D., & Allamandola, L. J. 2013, ApJ, 769, 117
Boersma, C., Hony, S., & Tielens, A. G. G. M. 2006, A&A, 447, 213
Boersma, C., Mattioda, A. L., Bauschlicher, C. W., et al. 2009, ApJ, 690, 1208
Boogert, A. C. A., Gerakines, P. A., & Whittet, D. C. B. 2015, ARA&A, 53, 541
Boogert, A. C. A., Huard, T. L., Cook, A. M., et al. 2011, ApJ, 729, 92
Boogert, A. C. A., Pontoppidan, K. M., Knez, C., et al. 2008, ApJ, 678, 985
Boogert, A. C. A., Pontoppidan, K. M., Lahuis, F., et al. 2004, ApJS, 154, 359
Bouwman, J., Boersma, C., Bulak, M., et al. 2020, A&A, 636, A57
Bouwman, J., Mattioda, A. L., Linnartz, H., & Allamandola, L. J. 2011, A&A, 525, A93
Bregman, J. D., Hayward, T. L., & Sloan, G. C. 2000, ApJL, 544, L75
Brooke, T. Y., Sellgren, K., & Geballe, T. R. 1999, ApJ, 517, 883
Brooke, T. Y., Sellgren, K., & Smith, R. G. 1996, ApJ, 459, 209
Buss, R. H., Tielens, A. G. G. M., & Snow, T. P. 1991, ApJ, 372, 281
Cardelli, J. A., Meyer, D. M., Jura, M., & Savage, B. D. 1996, ApJ, 467, 334
Cazaux, S., Arribard, Y., Egorov, D., et al. 2019, ApJ, 875, 27
Cook, A. M., Ricca, A., Mattioda, A. L., et al. 2015, ApJ, 799, 14
Cruz-Diaz, G. A., Erickson, S. E., da Silveira, E. F., et al. 2019, ApJ, 882, 44
de Barros, A. L. F., Mattioda, A. L., Ricca, A., Cruz-Diaz, G. A., & Allamandola, A. L. 2017, ApJ, 848, 112
Draine, B. T., & Li, A. 2007, ApJ, 657, 810
Dwek, E., Arendt, R. G., Fixsen, D. J., et al. 1997, ApJ, 475, 565
Galliano, F., Madden, S. C., Tielens, A. G. G. M., Peeters, E., & Jones, A. P. 2008, ApJ, 679, 310
Garkusha, I., Fulara, J., & Maier, J. P. 2012, JMoSt, 1025, 147
Gibb, E. L., Whittet, D. C. B., Schutte, W. A., et al. 2000, ApJ, 536, 347
Gillett, F. C., Forrest, W. J., & Merrill, K. M. 1973, ApJ, 183, 87
Hardegree-Ullman, E. E., Gudipati, M. S., Boogert, A. C. A., et al. 2014, ApJ, 784, 172
Hayatsu, R., Matsuoka, S., Anders, E., Scott, R., & Studier, M. 1977, GeCoA, 41, 132
Hony, S., van Kerckhoven, C., Peeters, E., et al. 2001, A&A, 370, 1030
Hudgins, D. L., & Allamandola, L. J. 1995a, JPhCh, 99, 3033
Hudgins, D. L., & Allamandola, L. J. 1995b, JPhCh, 99, 8978

Hudgins, D. L., & Sandford, S. A. 1998a, JPCA, 102, 329
Hudgins, D. L., & Sandford, S. A. 1998b, JPCA, 102, 353
Hudgins, D. L., & Sandford, S. A. 1998c, JPCA, 102, 344
Hudgins, D. L., Sandford, S. A., & Allamandola, L. J. 1994, JPhCh, 98, 4243
Hudgins, D. M., & Allamandola, L. J. 1997, JPCA, 101, 3472
Hudgins, D. M., Bauschlicher, C. W., & Allamandola, L. J. 2005, ApJ, 632, 316
Hudgins, D. M., Bauschlicher, C. W., Allamandola, L. J., & Fetzer, J. C. 2000, JPCA, 104, 3655
Joblin, C., Boissel, P., Leger, A., D'Hendecourt, L., & Defourneau, D. 1995, A&A, 299, 835
Joblin, C., D'Hendecourt, L., Leger, A., & Defourneau, D. 1994, A&A, 281, 923
Keane, J. V., Tielens, A. G. G. M., Boogert, A. C. A., Schutte, W. A., & Whittet, D. C. B. 2001, A&A, 376, 254
Kessler, M. F., Steinz, J. A., Anderegg, M. E., et al. 1996, A&A, 315, L27
Kim, H. S., Wagner, D. R., & Saykally, R. J. 2001, PhRvL, 86, 5691
Langhoff, S. R. 1996, JPhCh, 100, 2819
Lawson, C. L., & Hanson, R. J. 1974, Solving Least Squares Problems (Englewood Cliffs, NJ: Prentice-Hall)
Leech, K., Kester, D., Shipman, R. et al. (ed.) 2003, The ISO Handbook, Vol. 5, SWS—The Short Wavelength Spectrometer (Paris: ESA)
Li, A. 2020, NatAs, 4, 339
Li, A., & Draine, B. T. 2001, ApJ, 554, 778
Mackie, C. J., Chen, T., Candian, A., Lee, T. J., & Tielens, A. G. G. M. 2018, JChPh, 149, 134302
Mattioda, A. L., Allamandola, L. J., & Hudgins, D. M. 2005a, ApJ, 629, 1183
Mattioda, A. L., Bauschlicher, C. W., Bregman, J. D., et al. 2014, AcSpA, 130, 639
Mattioda, A. L., Bauschlicher, C. W., Ricca, A., et al. 2017, AcSpA, 181, 286
Mattioda, A. L., Hudgins, D. M., & Allamandola, L. J. 2005b, ApJ, 629, 1188
Mattioda, A. L., Hudgins, D. M., Bauschlicher, C. W., & Allamandola, L. J. 2005c, AdSpR, 36, 156
Mattioda, A. L., Hudgins, D. M., Bauschlicher, C. W., Rosi, M., & Allamandola, L. J. 2003, JPCA, 107, 1486
Mattioda, A. L., Ricca, A., Tucker, J., Bauschlicher, C. W., & Allamandola, L. J. 2009, ApJ, 137, 4054
Mattioda, A. L., Rutter, L., Parkhill, J., et al. 2008, ApJ, 680, 1243
Montillaud, J., Joblin, C., & Toublanc, D. 2013, A&A, 552, A15
Mulas, G., Malloci, G., Joblin, C., & Toublanc, D. 2006, A&A, 460, 93
Oomens, J., van Roij, A. J. A., Meijer, G., & von Helden, G. 2000, ApJ, 542, 404
Peeters, E., Allamandola, L. J., Hudgins, D. M., Hony, S., & Tielens, A. G. G. M. 2004, in ASP Conf. Ser. 309: Astrophysics of Dust, ed. A. N. Witt, G. C. Clayton, & B. T. Draine (San Francisco, CA: ASP), 141
Peeters, E., Berné, O., Habart, E. & ERS-PDR Team 2018, JWST ERS Program ID1288, http://astropah-news.strw.leidenuniv.nl/AstroPAH_0049.pdf
Peeters, E., Hony, S., van Kerckhoven, C., et al. 2002, A&A, 390, 1089
Puget, J. L., & Leger, A. 1989, ARA&A, 27, 161
Ricca, A., Bauschlicher, C. W., Mattioda, A. L., Boersma, C., & Allamandola, L. J. 2010, ApJ, 709, 42
Rosenberg, M. J. F., Berné, O., & Boersma, C. 2014, A&A, 566, L4
Rosenberg, M. J. F., Berné, O., Boersma, C., Allamandola, L. J., & Tielens, A. G. G. M. 2011, A&A, 532, A128
Sandford, S. A., & Allamandola, L. J. 1993, ApJ, 417, 815
Schutte, W. A., Gerakines, P. A., Geballe, T. R., van Dishoeck, E. F., & Greenberg, J. M. 1996a, A&A, 309, 633
Schutte, W. A., Tielens, A. G. G. M., Whittet, D. C. B., et al. 1996b, A&A, 315, L333
Sellgren, K. 1984, ApJ, 277, 623
Sellgren, K., Smith, R. G., & Brooke, T. Y. 1994, ApJ, 433, 179
Shannon, M. J., & Boersma, C. 2018, in Proc. 17th Python in Science Conf., ed. F. Akici et al., 99, doi:10.25080/Majora-4af1f417-00f
Smith, J. D. T., Draine, B. T., Dale, D. A., et al. 2007, ApJ, 656, 770
Speck, A., & Barlow, M. J. 1997, Ap&SS, 251, 115
Stein, S. 1978, JPhCh, 82, 566
Tielens, A. G. G. M. 2008, ARA&A, 45, 289
Tielens, A. G. G. M., Tokunaga, A. T., Geballe, T. R., & Baas, F. 1991, ApJ, 381, 181
Tsuge, M., Bahou, M., Wu, Y.-J., Allamandola, L., & Lee, Y.-P. 2016, ApJ, 825, 96
Vala, M., Szczepanski, J., Pauzat, F., et al. 1994, JPhCh, 98, 9187
van Diedenhoven, B., Peeters, E., van Kerckhoven, C., et al. 2004, ApJ, 611, 928
van Dishoeck, E. F. 2004, ARA&A, 42, 119
Weisman, J. L., Mattioda, A., Lee, T. J., et al. 2005, PCCP, 7, 109